Solution-Phase Synthesis of Vanadium Intercalated 1T'-WS₂ with Tunable Electronic Properties

Kuixin Zhu, Yiyin Tao, Daniel E. Clark, Wei Hong, Christina W. Li*

Department of Chemistry, Purdue University, West Lafayette, IN 47907, USA.

*Email: christinawli@purdue.edu

ABSTRACT: Metal ion intercalation into Group VI transition metal dichalcogenides enables control over their carrier transport properties. In this work, we demonstrate a low-temperature, solution-phase synthetic method to intercalate cationic vanadium complexes into bulk WS₂. Vanadium intercalation expands the interlayer spacing from 6.2 Å to 14.2 Å and stabilizes the 1T' phase of WS₂. Kelvin-probe force microscopy measurements indicate that vanadium binding in the van der Waals gap causes in increase in the Fermi level of 1T'-WS₂ by 80 meV due to hybridization of vanadium 3d orbitals with the conduction band of the TMD. As a result, the carrier type switches from p-type to n-type, and carrier mobility increases by an order of magnitude relative to the Li-intercalated precursor. Both the conductivity and thermal activation barrier for carrier transport are readily tuned by varying the concentration of VCl₃ during the cation-exchange reaction.

Keywords: transition metal dichalcogenides, two-dimensional materials, intercalation, Hall effect, conductivity

Two-dimensional materials are attractive for nanoscale, flexible electronic devices, but greater control over their electronic properties--band gap, carrier mobility and density—is needed for more widespread application.¹⁻⁷ The highly anisotropic structure of transition metal dichalcogenides (TMDs) enables incorporation of guest atoms into the van der Waals gap without disrupting the chemical bonds in the two-dimensional layer. These intercalated atoms can have dramatic effects on the electronic properties of the TMD through electron transfer and orbital hybridization.⁸⁻¹⁶

In most cases, the intercalation of a metal atom or cation is thermodynamically-driven by electron-transfer into the conduction band of the TMD, either from the intercalant atom itself or from an external reductant or reducing potential. The majority of studies in the literature have focused on alkali ion intercalants because electron transfer is very favorable from the reducing alkali $\rm M^0$ to the TMD. Some non-alkali metal atoms can also be intercalated in this fashion, but the possible intercalant-TMD combinations as well as the extent of intercalation are limited by the relative energies of metal atom oxidation and the conduction band of the TMD. $^{\rm 31-35}$

The charge-transfer intercalation strategy is particularly challenging for Group VI metal sulfides (MoS₂, WS₂) because of their high conduction band energies,^{36,37} and only alkali metals have been capable of intercalating in high concentration.³⁸⁻⁴⁴ To further functionalize the TMD, alkali-intercalated structures can undergo subsequent exchange with guest species through an exfoliation and restacking process.⁴⁵ While this method enables a wide diversity of intercalants—including cations,

organic molecules, inorganic complexes, and polymers—the exfoliation step in water significantly alters the morphological properties of the TMD and quenches the negative charge introduced by the alkali reductant. $^{46\text{-}60}$

Electronically, alkali-intercalated MoS₂ and WS₂ have increased carrier densities and mobilities relative to the unintercalated TMD due to alkali electron transfer and conversion to the 1T' phase.^{26,61} However, these structures are highly unstable to ambient atmosphere or protic solvent because the negative charge is entirely confined on the TMD.^{29,62,63} In this work, we develop a solution-phase method to intercalate transition metal ions into bulk WS₂ through charge-transfer intercalation of Li followed by cation exchange to vanadium (**Figure 1a**). In doing so, we are able to stabilize the electronically-activated 1T' phase of WS₂ and further enhance carrier mobility through hybridization of the vanadium 3d orbitals into the conduction band. Synthesis of 1T-WS₂ substitutionally-doped with V atoms was also demonstrated recently using chemical vapor deposition.⁶⁴

Bulk WS₂ is first reductively activated and intercalated with Li⁺ using n-butyllithium (n-BuLi) based on literature methods.²⁷ Zeta-potential measurements of the lithiated WS₂ (Li_xWS₂) immediately after n-BuLi treatment reveals a strong anionic charge (–70 mV), which dissipates rapidly if exposed to O₂ and slowly if exposed to polar solvents under airfree conditions (**Figure S2**). To maximize the electrostatic interaction between the anionic TMD sheets and vanadium cations, we carry out the cation exchange reaction between Li_xWS₂ powder and V³⁺ precursors in N-methylformamide (NMF) solution for just 1 hour under N₂.

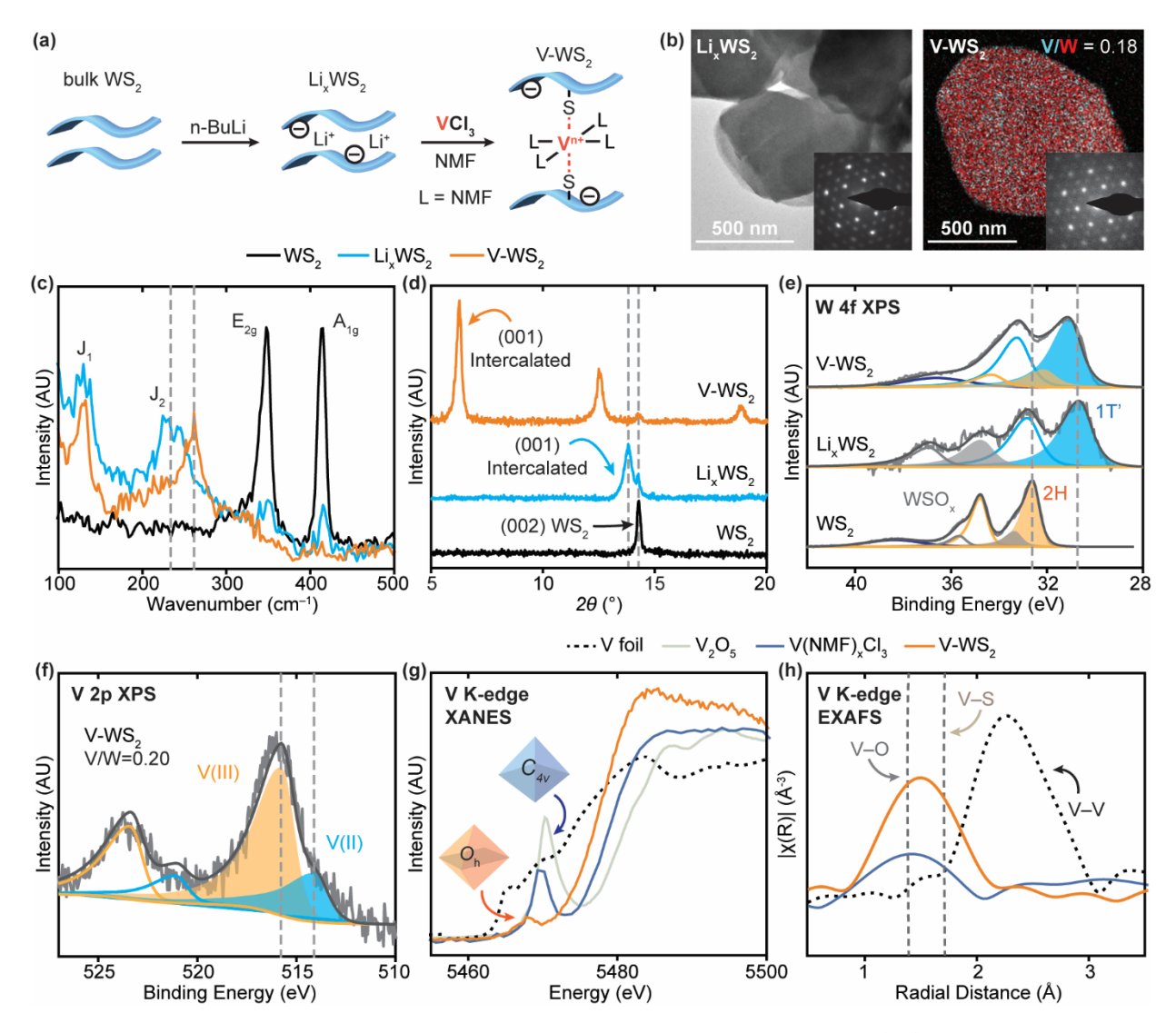


Figure 1. (a) Schematic for the synthesis of intercalated V-WS₂. (b) TEM image and SAED pattern of Li_xWS₂ (left), EDS map and SAED pattern of V-WS₂ (right). (c) Raman spectra, (d) powder XRD patterns, and (e) W 4f XPS spectra of 2H-WS₂, Li_xWS₂, and V-WS₂. (f) V 2p XPS spectrum for V-WS₂. (g) V K-edge XANES spectra and (h) V K-edge EXAFS spectra for V-WS₂ and control samples.

WS2 undergoes significant structural changes during this two-step intercalation process. During n-BuLi activation, we observe a phase transition from the 2H phase to the distorted 1T' phase based on the $2a \times 2a$ superlattice spots observed in the transmission electron microscope (TEM) selected-area electron diffraction (SAED) patterns (Fig**ure 1b**). 40 Raman spectra show the loss of the characteristic E_{2g} and A_{1g} vibrational modes of 2H-WS₂ and the appearance of the J₁ and J₂ modes of 1T'-WS2 (Figure 1c).65-67 Because the 1T' phase has a narrow bandgap (~110 meV),68,69 diffuse-reflectance UV-Vis spectra show no absorption features (Figure S3). X-ray photoelectron spectra (XPS) of the W 4f peaks exhibit a characteristic shift to lower binding energy due to the phase transition (**Figure 1e**).⁷⁰ Powder X-ray diffraction (XRD) reveals an expansion of the interlayer galleries after lithiation. The (00n) peak shifts from 14.3° in bulk WS₂ to 13.9° in Li_xWS₂, an increase in interlayer spacing from 6.18 Å to 6.36 Å (Figure 1d). By comparing the relative areas of the two (00n) peaks, we estimate that 19% of the sample remains unintercalated due to the diffusional constraints of Li in large WS₂ microparticles.⁷¹

Upon reaction of LixWS2 with 2.0 equiv. VCl3, a further shift in the (00n) peak to 6.25° is observed, and the unintercalated WS₂ diffraction peak is suppressed (Figure 1d). The relative area of the two peaks indicates that 92% of the WS₂ material is intercalated with the large, solvated Vⁿ⁺ complex. The observed interlayer distance of 14.2 Å is comparable to previous examples of hydrated Na+ intercalated into MoS2. 56 A V:W atomic ratio of 0.18 is observed by energy-dispersive X-ray spectroscopy (EDS) and X-ray fluorescence (XRF) (Table S1), and V atoms are evenly distributed across the lateral surface of the WS₂ microparticle based on EDS mapping (Figure 1b, S4). Elemental analysis using XPS reveals a near-surface V:W ratio of 0.20 (**Table S1**), similar to the bulk ratio, which suggests that V species are also uniformly distributed throughout the thickness of the WS2 sheet. XPS on the V 2p region shows that 30% of intercalants are partially reduced from V^{3+} to V^{2+} by the negatively charged Li_xWS₂ sheets (Figure 1f). Correspondingly, a slight shift in the W 4f XPS peak to higher binding energy is observed due to consumption of excess electrons by V complexes (Figure 1e).25

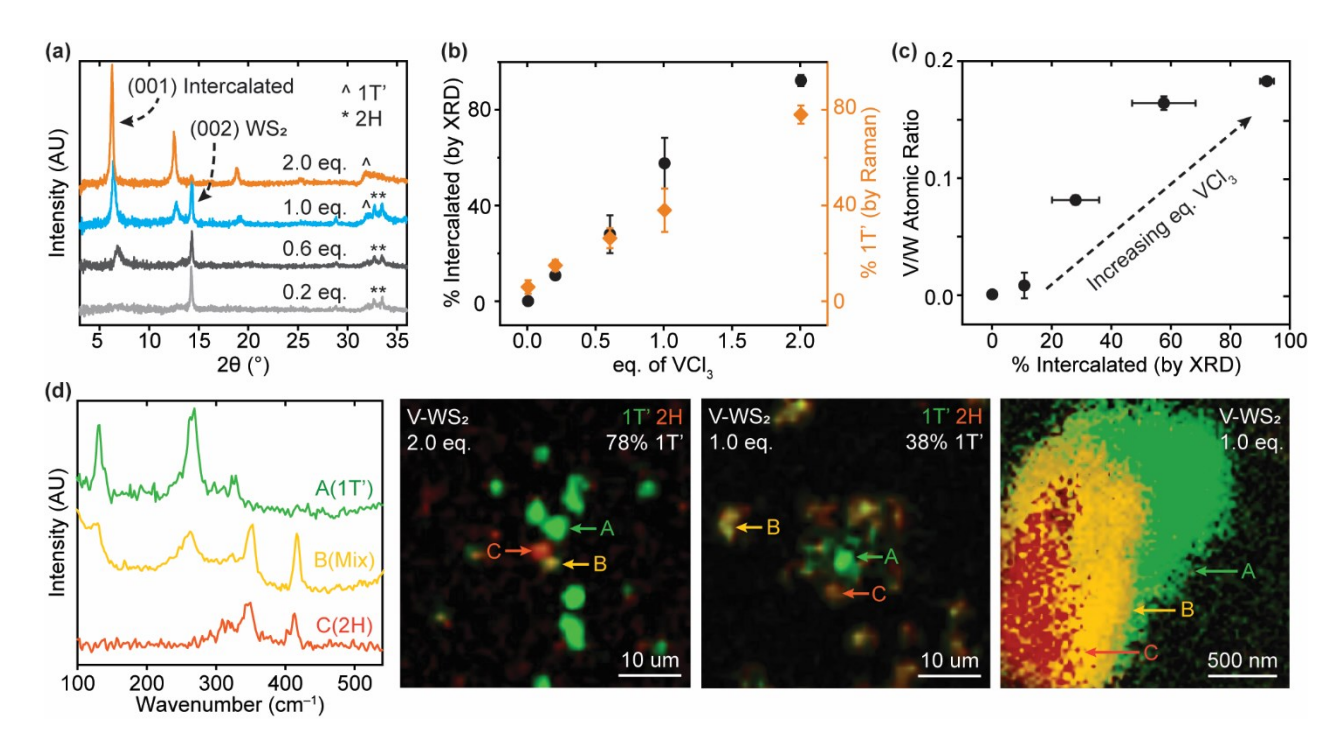


Figure 2. (a) Powder XRD patterns of V-WS₂ synthesized with varying equivalents of VCl₃. (b) The percentage of the sample intercalated with V (left axis) and in the IT' phase (right axis) as a function of VCl₃ equiv. (c) V/W atomic ratio vs. percentage of V-intercalated WS₂. (d) Representative Raman spectra of 1T' (green), mixed phase (yellow), and 2H (red) regions and Raman maps of 2.0 and 1.0 equiv. V-WS₂.

Raman spectra reveal an interesting change in the WS_2 interlayer coupling strength after V intercalation (**Figure 1c**). V-WS $_2$ remains predominantly in the distorted 1T' phase, but a significant blue-shift is observed in the J_2 mode, which represents a linear combination of the out-of-plane A_{1g} mode and the longitudinal acoustic mode at the M point in the Brillouin zone. The shift from 240 cm $^{-1}$ in $L_{1g}WS_2$ to 260 cm $^{-1}$ in V-WS $_2$ indicates a strengthening of the interlayer coupling, likely because $V^{2/3+}$ ions can coordinatively bridge two WS $_2$ layers through the van der Waals gap. The shift from 240 cm $^{-1}$ in V-WS $_3$ layers through the van der Waals gap. The shift from 240 cm $^{-1}$ in the Waals gap. The shift from 240 cm $^{-1}$ in V-WS $_3$ layers through the van der Waals gap. The shift from 240 cm $^{-1}$ in V-WS $_3$ layers through the van der Waals gap.

V K-edge X-ray absorption near edge spectroscopy (XANES) provides further information on the oxidation state and local coordination geometry of V atoms in V-WS₂ (Figure 1g). We compare the XANES spectrum to those of V metal foil, bulk V₂O₅, and the V precursor, prepared by dissolving anhydrous VCl₃ in NMF. The solvated precursor complex, V(NMF)_xCl₃, has V K-edge energy of 5479.04 eV, which is characteristic of oxygen-coordinated V³⁺ molecular complexes.⁷⁵ Upon intercalation into WS2, the V K-edge energy red-shifts by 1.69 eV, consistent with partial reduction to V²⁺. More interestingly, the intensity of the pre-edge feature at the V K-edge reports on the vanadium local coordination geometry. ⁷⁶ Crystalline V₂O₅ comprises only square pyramidal V⁵⁺ ions and shows the highest intensity pre-edge feature at 5469.89 eV. The precursor V(NMF)_xCl₃ has an intermediate pre-edge intensity due to formation of a mixture of 4-6 coordinate complexes in solution. Critically, the V atoms in V-WS2 show a weak pre-edge feature at 5465.77 eV, suggesting that the centrosymmetry of the V ion increases upon intercalation to adopt a pseudo-octahedral geometry through interaction with the WS₂ basal planes.

Further evidence of the change in V coordination is observed in the X-ray absorption fine structure (EXAFS) (**Figure 1h**). Both V-WS₂ and the V(NMF)_xCl₃ complex have their first coordination sphere scattering peaks at short radial distance, as expected for oxygen-based ligands bound to $V^{2/3+}$ (**Table S2, Figure S5**).⁷⁷ An increase in amplitude of the R-space peak for V-WS₂ compared to its precursor complex reflects an increase in coordination number. In addition, a slight shift to longer radial distance is observed. In literature vanadium structures, V–S bonds tend to be ~0.28 Å longer than V–O bonds (**Table S3**), and the small increase in average bond length for V-WS₂ may arise from the inclusion of S ligands in the first coordination sphere.

Varying the quantity of VCl₃ precursor in the cation-exchange step enables systematic variation of the intercalated V-WS₂ fraction. The XRD (001) peak position for the V-intercalated WS₂ remains at 6.25° regardless of the VCl₃ concentration, but the relative areas of the intercalated and non-intercalated (00n) peaks vary significantly (**Figure 2a**). The percentage of intercalated WS₂ drops from 92% at 2.0 equiv. VCl₃ to 58%, 28%, and 11% at 1.0, 0.6, and 0.2 equiv., respectively (**Figure 2b**). As controls, we stir the Li_xWS₂ sample in pure NMF or MgCl₂-containing solutions to understand the role of solvent and cation identity in the intercalation process. In NMF alone, Li⁺ species diffuse out of the interlayer galleries, and no expanded d-spacing is observed in the XRD (**Figure S6a**). Mg²⁺, which has similar solvated ionic radius to V³⁺, shows full intercalation and similar interlayer spacing to the V-WS₂ samples (**Figure S6b**).

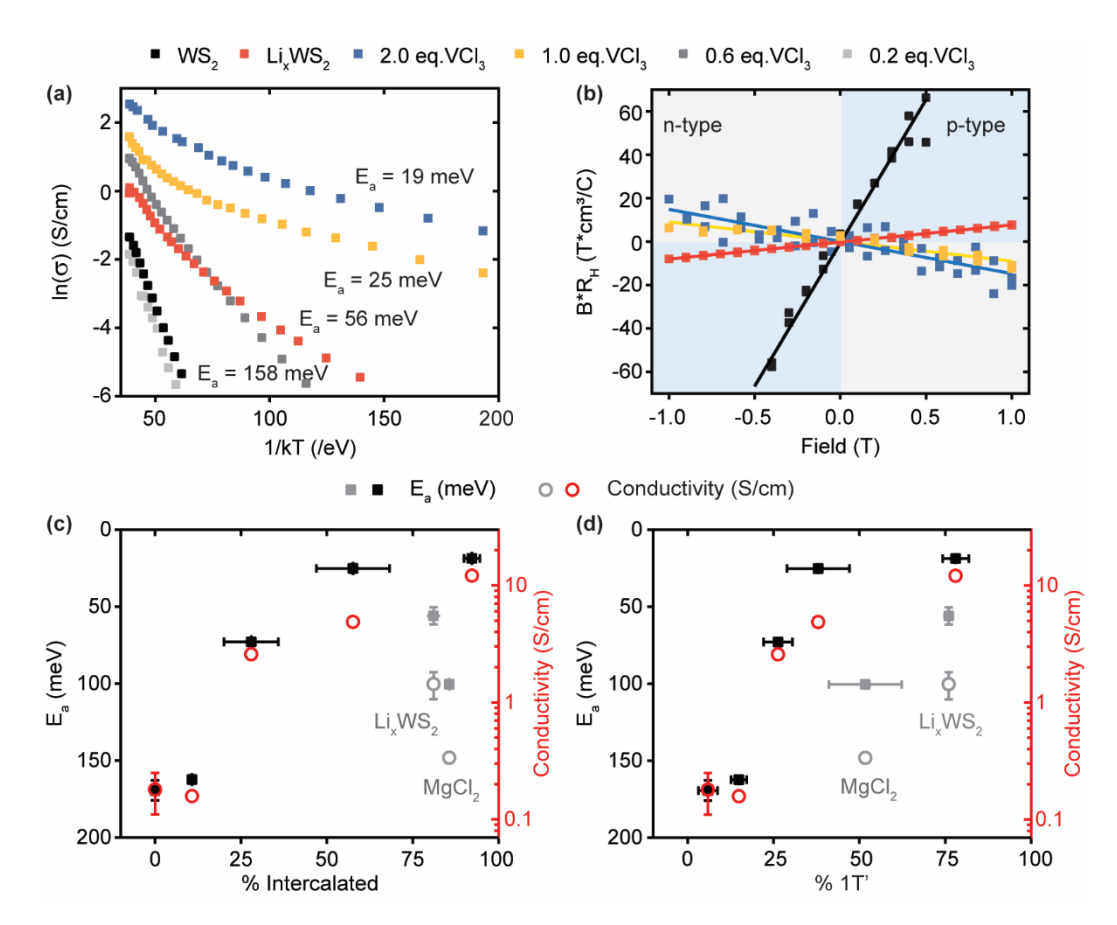


Figure 3. Electronic characterization of V-WS₂ and control samples. (a) Temperature-dependent conductivity plotted as $\ln(\sigma)$ vs. 1/kT and (b) Hall effect measurements. (c, d) Analysis of the carrier activation energy and room-temperature conductivity as a function of the (c) degree of intercalation and (d) 1T' phase retention.

During the cation-exchange reaction, WS2 sheets exhibit varying degrees of phase reversion from pure 1T' in Li_xWS₂ to the 2H phase after stirring in NMF solution.²⁸ We utilize Raman mapping experiments to quantify the area percent of 1T' and 2H phases using the characteristic peaks at 260 cm⁻¹ and 414 cm⁻¹, respectively (**Figure 2d, S7**). The 2.0 equiv. V-WS2 sample shows the highest degree of 1T' phase retention (78%). The majority of WS₂ microparticles remain in the 1T' phase (A) with a small number of particles exhibiting a mixture of phases (B) or the pure 2H phase (C). As the concentration of VCl₃ precursor is reduced, a greater degree of phase reversion occurs (Figure 2b), but some phasepure 2H and 1T' particles remain in every sample. Higher resolution mapping of mixed-phase particles in the 1.0 equiv. V-WS₂ sample shows an anisotropic distribution of phases even at the single sheet level (Figure 2d, S8a), and comparable spatial heterogeneity is observed for the V/W atomic ratio in EDS mapping (**Figure S8b-c**). These observations suggest that V intercalation is tied to phase stability and that a kinetic barrier exists for the phase reversion reaction, which depends on cation diffusion and microparticle edge structure. In the NMF-only control sample, WS₂ converts entirely back to the 2H phase because there are no V ions in solution to replace the deintercalating Li⁺ (Figure S7, S9). Mg²⁺ shows an intermediate ability to stabilize the 1T' phase, retaining 51%.

Surprisingly, the quantity of V in the sample determined by XRF does not scale directly with the percentage of intercalated WS₂. (**Figure 2c**) The V/W ratio increases from 0.02 to 0.16 from 0.2 equiv. to 1.0 equiv.

 VCl_3 but plateaus at that level from 1.0 equiv. to 2.0 equiv. despite the continued increase in intercalated WS_2 percentage by XRD. The fraction of reduced V^{2+} species by XPS also remains relatively constant from 1.0 equiv. to 2.0 equiv. (**Figure S10**). The discrepancy between intercalated and total V suggests that intercalation occurs in a stepwise fashion, in which V^{3+} is first reduced and adsorbed at the edges of the WS₂ microparticles followed by diffusion into the interlayer galleries, the latter of which becomes more favorable at higher concentrations of V precursor.

To understand the role of V intercalants on the electronic properties of WS₂, we conducted temperature-dependent conductivity and Hall effect measurements on pressed pellets in a 4-point van der Pauw configuration. While electronic transport measurements on pellets will necessarily be convoluted by grain boundaries, the presence of mixed phases, other structural heterogeneity, and the narrow band gap of the 1T' phase, comparisons between Li_xWS₂ and V-WS₂ samples still provide useful structure-property correlations. Temperature-dependent conductivity measurements from 300 K to 60 K (Figure S12) illustrate that carrier transport is a thermally-activated process governed by the Arrhenius equation. Measurements on key samples were carried out in triplicate to insure the reproducibility of our synthetic method and pellet preparation (Table S4). Figure 3a shows Arrhenius plots for V-doped WS₂ samples and undoped controls. We also obtained Hall effect measurements to determine the carrier type, density, and mobility for a subset of samples (Figure 3b, Table S5).

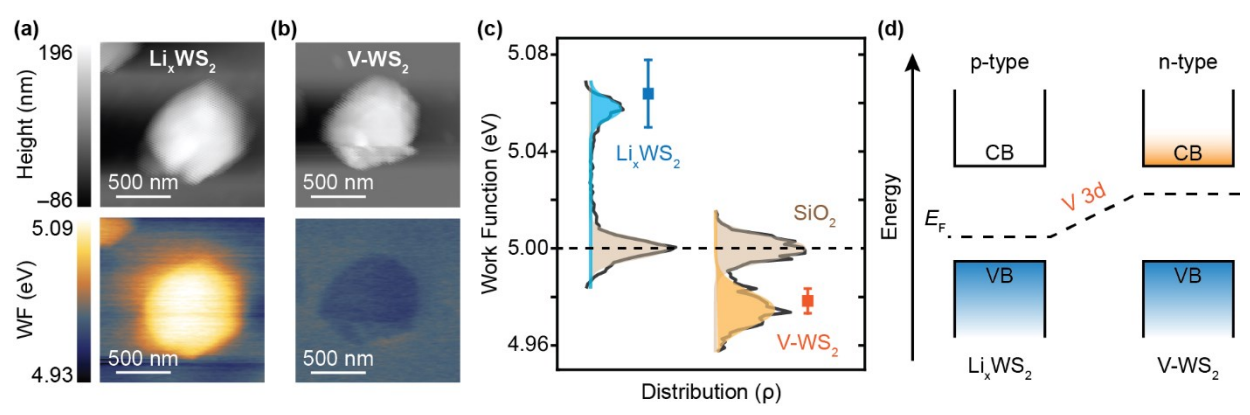


Figure 4. Kelvin-Probe Force Microscope (KPFM) measurements showing height and work function maps of (a) Li_xWS₂ and (b) V-WS₂. (c) Histograms of the measured work function values extracted from the spatial map. (d) Band structure diagram illustrating the change in Fermi level with V intercalation.

Congruent with previous polycrystalline measurements in the literature (**Table S6**), the untreated 2H-WS $_2$ powder is a p-type semiconductor with carrier density of 4.6 * 10^{16} cm $^{-3}$, and mobility of 24 cm 2 V $^{-1}$ s $^{-1}$. The room temperature conductivity of the pellet is 0.18 S cm $^{-1}$, and the carrier transport activation energy is 158 meV. Upon lithiation, the conductivity increases to 1.4 S cm $^{-1}$, and E_a drops to 56 meV. Li-intercalated WS $_2$ remains a p-type semiconductor, exhibiting an order of magnitude increase in carrier density (9.2 * 10^{17} cm $^{-3}$) and a slight drop in carrier mobility (10 cm 2 V $^{-1}$ s $^{-1}$) relative to the unlithiated sample. The electronic properties after lithiation stem from both the 2H to 1T $^{\prime}$ phase change as well as the injection of electrons from n-BuLi. 26,78 The much smaller bandgap of 1T $^{\prime}$ -WS $_2$ compared to 2H-WS $_2$ leads to the lower carrier activation energy and higher carrier density at 300 K.

The 2.0 equiv. V-WS2 sample, which has near complete formation of the intercalated structure and retention of the 1T' phase, shows another order of magnitude increase in room temperature conductivity up to 12.1 S cm⁻¹ and decrease in E_a to 19 meV. Intriguingly, the dominant carrier type switches from p-type to n-type with carrier density of 4.2 * 10¹⁷ cm⁻³, and mobility of 179 cm² V⁻¹s⁻¹. We hypothesize that hybridization of $V^{2/3+}$ d-electrons with the conduction band of 1T'-WS₂ shifts the Fermi level towards the conduction band, thereby making electrons the dominant carrier and reducing the carrier transport activation barrier.⁷⁹ The V-intercalated WS₂ samples prepared with lower equivalents of VCl₃ exhibit electron transport properties commensurate with the amount of V intercalated into the WS2 sheets. Using 1 equiv. VCl3, the carrier mobility and conductivity drop relative to the fully intercalated sample to $58 \text{ cm}^2 \text{V}^{-1} \text{s}^{-1}$ and 6.5 S cm^{-1} , respectively, while E_a and carrier density remain unchanged. Conductivity further decreases and Ea increases at 0.6 and 0.2 equiv. of VCl₃, falling near that of Li_xWS₂ and 2H-WS2, respectively.

For the Li_xWS_2 control stirred with NMF alone, the electronic and structural properties are similar to 2H-WS₂ (**Figure S6**). In general, samples that lack V intercalants and revert to the 2H phase exhibit low conductivity and high E_a values (**Figure 3c-d**). Increasing the concentration of VCl₃ precursor increases both intercalation and 1T' percentage simultaneously, leading to improved electronic properties. Mg-WS₂ provides a useful control for a fully-intercalated sample containing a cation without d-orbitals capable of hybridizing with the WS₂ conduction band. In this case, despite the 86% intercalation, the conductivity remains very low at 0.33 S cm⁻¹, in the same regime as the poorly intercalated V samples. Both the Li⁺ and Mg²⁺-intercalated WS₂ samples have lower conductivity and higher E_a relative to V-WS₂ samples at similar levels of intercalation and 1T' phase retention, suggesting that 3d

electrons in the V-intercalants are crucial toward modulating the electronic properties of WS_2 .

Pressed-pellet van der Pauw measurements provide the average electronic properties of the V-WS₂ powder but may be convoluted by charge trapping and energetic barriers at grain boundaries.80 To directly assess the electronic influence of V intercalants on the WS2 band structure, we performed single-particle Kelvin Probe Force Microscopy (KPFM) measurements on bulk WS2, LixWS2, and 2.0 equiv. V-WS2 to determine the work function of each sample.^{81,82} Samples were spun-coat onto a SiO₂-passivated Si wafer, and both the sample height and contact potential difference (CPD) between the tip and the surface were measured (Figure 4a-b, S13-14). Morphologically, all samples comprise microparticles with lateral diameter of ~1 µm and thickness of 100-200 nm (**Figure S15**). To obtain the work function, we mapped 3 areas on each sample, each of which contained one WS2 particle surrounded by bare SiO₂. A CPD histogram was generated from each area, which was fit to two Gaussians to obtain the average CPD of the SiO2 substrate as well as the WS₂ sheet (**Figure 4c, S13-14**). Because the absolute value of the CPD depends on the work function of the tip and varies across measurements, the SiO₂ substrate is used as a reference with known work function of 5.00 eV to convert the CPD data into work function values. 83,84

The results show that bulk WS₂ has an average work function of 5.01 eV, similar to values reported in the literature. Some spatial variation is observed moving from the edges to the center of the microsheet, which is consistent with a gradient in the spatial distribution of defects (**Figure S13**). After n-BuLi treatment, the work function of Li_xWS₂ increases to 5.06 eV, corresponding to a 50 meV drop in the Fermi level, because the distorted 1T' phase has a lower conduction band minimum and smaller band gap than the 2H phase (**Figure 4a, c**). An adium intercalation results in a reduction in work function to 4.98 eV and correspondingly, an 80 meV increase in Fermi level compared to Li_xWS₂ (**Figure 4b, c**). Given that V-WS₂ and Li_xWS₂ are both in the 1T' phase, we postulate that the interaction of V 3d electrons with the 1T' WS₂ conduction band shifts the Fermi level toward the conduction band by 80 meV and leads to the observed change in carrier type from p-type to n-type (**Figure 4d**).

In conclusion, we have developed a solution-phase synthetic method to activate and intercalate WS_2 with solvated V ions, which enables wideranging control over the carrier transport properties of V-intercalated 1T'-WS₂. Detailed structural analysis using XRD and Raman spectroscopy shows that intercalation of V increases the interlayer spacing of WS₂ by 8.02 Å while strengthening the interlayer coupling. Electronically, the carrier type switches from p-type to n-type, and the conductivity increases by an order of magnitude in V-WS₂ compared to 1T'-

 Li_xWS_2 . Based on single-sheet KPFM measurements, these electronic changes stem from an increase in the Fermi level by 80 meV due to the interaction of V 3d orbitals with the WS_2 conduction band. This report provides the first example of charge-transfer intercalation of a solvated transition metal complex into the van der Waals gap of bulk WS_2 , showing a strong electronic hybridization despite its relatively disordered structure. This low-temperature, solution-phase synthetic strategy has the potential to expand the compositional diversity of transition-metal intercalated TMDs and enable facile control over their electronic properties.

ASSOCIATED CONTENT

Supporting Information

The Supporting Information is available free of charge on the ACS Publications website.

Additional experimental details, materials, synthetic methods, physical characterization methods, electronic characterization methods, and supplementary figures and tables (PDF)

AUTHOR INFORMATION

Corresponding Author

Christina W. Li: christinawli@purdue.edu

Notes

The authors declare no competing financial interests.

ACKNOWLEDGMENT

This work was supported by the National Science Foundation (CHE-2106450). We acknowledge Zhifan Ke and Professor Jianguo Mei for their help with Au evaporation. We thank Tania Class Martinez and Professor Rajamani Gounder for assistance with DRUV–Vis data collection. We thank Dr. Neil R. Dilley for his help with PPMS electronic transport measurements. We acknowledge Dr. Yujia Ding, Dr. Carlo Segre, and Dr. Joshua Wright for their assistance with XAS experiments. XAS data was collected at beamline 10-BM at the Advanced Photon Source (APS), Argonne National Laboratory. Use of the APS is supported by the U.S. Department of Energy, Office of Science, Office of Basic Energy Sciences, under Contract DE-AC02-06CH11357. MRCAT operations are supported by the Department of Energy and the MRCAT member institutions. XPS data was obtained at the Surface Analysis Facility of the Birck Nanotechnology Center, Purdue University.

REFERENCES

- (1) Gong, C. H.; Zhang, Y. X.; Chen, W.; Chu, J. W.; Lei, T. Y.; Pu, J. R.; Dai, L. P.; Wu, C. Y.; Cheng, Y. H.; Zhai, T. Y.; Li, L.; Xiong, J. Electronic and Optoelectronic Applications Based on 2D Novel Anisotropic Transition Metal Dichalcogenides. *Adv. Sci.*, **2017**, *4*, 1700231.
- (2) Zeng, Q. S.; Liu, Z. Novel Optoelectronic Devices: Transition-Metal-Dichalcogenide-Based 2D Heterostructures. *Adv. Electron. Mater.*, **2018**, *4*, 1700335.
- (3) Song, X. F.; Guo, Z. X.; Zhang, Q. C.; Zhou, P.; Bao, W. Z.; Zhang, D. W. Progress of Large-Scale Synthesis and Electronic Device Application of Two-Dimensional Transition Metal Dichalcogenides. *Small*, **2017**, *13*, 1700098.
- (4) Radisavljevic, B.; Radenovic, A.; Brivio, J.; Giacometti, V.; Kis, A. Single-layer MoS₂ transistors. *Nat. Nanotechnol.*, **2011**, *6*, 147-150.

- (5) Das, S.; Chen, H. Y.; Penumatcha, A. V.; Appenzeller, J. High Performance Multilayer MoS₂ Transistors with Scandium Contacts. *Nano Lett.*, **2013**, *13*, 100-105.
- (6) Das, S.; Appenzeller, J. WSe₂ field effect transistors with enhanced ambipolar characteristics. *Appl. Phys. Lett.*, **2013**, 103, 103501
- (7) Wang, Z.; Li, R.; Su, C.; Loh, K. P. Intercalated phases of transition metal dichalcogenides. *SmartMat*, **2020**, *1*, e1013.
- (8) Friend, R. H.; Yoffe, A. D. Electronic-Properties of Intercalation Complexes of the Transition-Metal Dichalcogenides. *Adv. Phys.*, **1987**, *36*, 1-94.
- (9) Clark, W. B. Structural and photoemission studies of some transition metal intercalates of NbS₂. *J. Phys. C: Solid State Phys.*, **1976**, *9*, L693.
- (10) Morosan, E.; Zandbergen, H. W.; Dennis, B. S.; Bos, J. W. G.; Onose, Y.; Klimczuk, T.; Ramirez, A. P.; Ong, N. P.; Cava, R. J. Superconductivity in Cu_xTiSe₂. *Nat. Phys.*, **2006**, 2, 544-550.
- (11) Guzman, D. M.; Onofrio, N.; Strachan, A. First principles investigation of copper and silver intercalated molybdenum disulfide. *J. Appl. Phys.*, **2017**, *121*, 055703.
- (12) Chhowalla, M.; Shin, H. S.; Eda, G.; Li, L. J.; Loh, K. P.; Zhang, H. The chemistry of two-dimensional layered transition metal dichalcogenide nanosheets. *Nat. Chem.*, **2013**, *5*, 263-275.
- (13) Wu, Y.; Li, D.; Wu, C.-L.; Hwang, H. Y.; Cui, Y. Electrostatic gating and intercalation in 2D materials. *Nat. Rev. Mater.*, **2022**, *8*, 41-53.
- (14) Zhou, J.; Lin, Z.; Ren, H.; Duan, X.; Shakir, I.; Huang, Y.; Duan, X. Layered Intercalation Materials. *Adv. Mater.*, **2021**, 33, 2004557.
- (15) Wan, J. Y.; Lacey, S. D.; Dai, J. Q.; Bao, W. Z.; Fuhrer, M. S.; Hu, L. B. Tuning two-dimensional nanomaterials by intercalation: materials, properties and applications. *Chem. Soc. Rev.*, **2016**, *45*, 6742-6765.
- (16) Yuan, H. T.; Wang, H. T.; Cui, Y. Two-Dimensional Layered Chalcogenides: From Rational Synthesis to Property Control via Orbital Occupation and Electron Filling. *Acc. Chem. Res.*, **2015**, *48*, 81-90.
- (17) Whittingham, M. S. Chemistry of intercalation compounds: Metal guests in chalcogenide hosts. *Prog. Solid State Chem.*, **1978**, *12*, 41-99.
- (18) Jung, Y.; Zhou, Y.; Cha, J. J. Intercalation in two-dimensional transition metal chalcogenides. *Inorg. Chem. Front.*, **2016**, *3*, 452-463.
- (19) Nitsche, R.; Wild, P. Vapour growth of new single-crystalline phases in the system Cu-Nb-S. J. Cryst. Growth, **1968**, 3-4, 153-158.
- (20) Zhao, X.; Song, P.; Wang, C.; Riis-Jensen, A. C.; Fu, W.; Deng, Y.; Wan, D.; Kang, L.; Ning, S.; Dan, J.; Venkatesan, T.; Liu, Z.; Zhou, W.; Thygesen, K. S.; Luo, X.; Pennycook, S. J.; Loh, K. P. Engineering covalently bonded 2D layered materials by self-intercalation. *Nature*, **2020**, *581*, 171-177.
- (21) Zhang, J.; Sun, J.; Li, Y.; Shi, F.; Cui, Y. Electrochemical Control of Copper Intercalation into Nanoscale Bi₂Se₃. *Nano Lett.*, **2017**, *17*, 1741-1747.
- (22) Zeng, Z. Y.; Yin, Z. Y.; Huang, X.; Li, H.; He, Q. Y.; Lu, G.; Boey, F.; Zhang, H. Single-Layer Semiconducting Nanosheets: High-Yield Preparation and Device Fabrication. *Angew. Chem. Int. Ed.*, **2011**, *50*, 11093-11097.
- (23) Zhang, J. S.; Yang, A. K.; Wu, X.; van de Groep, J.; Tang, P. Z.; Li, S. R.; Liu, B. F.; Shi, F. F.; Wan, J. Y.; Li, Q. T.; Sun, Y. M.; Lu, Z. Y.; Zheng, X. L.; Zhou, G. M.; Wu, C. L.; Zhang, S. C.; Brongersma, M. L.; Li, J.; Cui, Y. Reversible and selective ion intercalation through the top surface of few-layer MoS₂. *Nat. Commun.*, **2018**, *9*, 5289.
- (24) He, Q.; Lin, Z.; Ding, M.; Yin, A.; Halim, U.; Wang, C.; Liu, Y.; Cheng, H. C.; Huang, Y.; Duan, X. In Situ Probing Molecular Intercalation in Two-Dimensional Layered Semiconductors. *Nano Lett.*, **2019**, *19*, 6819-6826.
- (25) Wang, C.; He, Q.; Halim, U.; Liu, Y.; Zhu, E.; Lin, Z.; Xiao, H.; Duan, X.; Feng, Z.; Cheng, R.; Weiss, N. O.; Ye, G.; Huang, Y. C.; Wu, H.; Cheng, H. C.; Shakir, I.; Liao, L.; Chen, X.; Goddard, W. A.; Huang, Y.; Duan, X. Monolayer atomic crystal molecular superlattices. *Nature*, **2018**, 555, 231-236.
- (26) Heising, J.; Kanatzidis, M. G. Exfoliated and restacked MoS₂ and WS₂: Ionic or neutral species? Encapsulation and ordering of hard electropositive cations. *J. Am. Chem. Soc.*, **1999**, *121*, 11720-11732.
- (27) Yang, D.; Frindt, R. F. Li-intercalation and exfoliation of WS₂. *J. Phys. Chem. Solids*, **1996**, *57*, 1113-1116.
- (28) Xiong, F.; Wang, H.; Liu, X.; Sun, J.; Brongersma, M.; Pop, E.; Cui, Y. Li Intercalation in MoS₂: In Situ Observation of Its Dynamics and Tuning Optical and Electrical Properties. *Nano Lett.*, **2015**, *15*, 6777-6784.
- (29) Py, M. A.; Haering, R. R. Structural Destabilization Induced by Lithium Intercalation in MoS₂ and Related Compounds. *Can. J. Phys.*, **1983**, *61*, 76-84.

- (30) Zak, A.; Feldman, Y.; Lyakhovitskaya, V.; Leitus, G.; Popovitz-Biro, R.; Wachtel, E.; Cohen, H.; Reich, S.; Tenne, R. Alkali metal intercalated fullerene-like MS_2 (M = W, Mo) nanoparticles and their properties. *J. Am. Chem. Soc.*, **2002**, *124*, 4747-4758.
- (31) Koski, K. J.; Wessells, C. D.; Reed, B. W.; Cha, J. J.; Kong, D.; Cui, Y. Chemical intercalation of zerovalent metals into 2D layered Bi₂Se₃ nanoribbons. *J. Am. Chem. Soc.*, **2012**, *134*, 13773-13779.
- (32) Wang, M.; Koski, K. J. Reversible chemochromic MoO₃nanoribbons through zerovalent metal intercalation. *ACS Nano*, **2015**, *9*, 3226-3233.
- (33) Gong, Y.; Yuan, H.; Wu, C. L.; Tang, P.; Yang, S. Z.; Yang, A.; Li, G.; Liu, B.; Van De Groep, J.; Brongersma, M. L.; Chisholm, M. F.; Zhang, S. C.; Zhou, W.; Cui, Y. Spatially controlled doping of two-dimensional SnS₂ through intercalation for electronics. *Nat. Nanotechnol.*, **2018**, *13*, 294-299.
- (34) Xie, L. S.; Husremović, S.; Gonzalez, O.; Craig, I. M.; Bediako, D. K. Structure and Magnetism of Iron- and Chromium-Intercalated Niobium and Tantalum Disulfides. *J. Am. Chem. Soc.*, **2022**, 144, 9525-9542.
- (35) Twitto, A.; Stern, C.; Poplinger, M.; Perelshtein, I.; Saha, S.; Jain, A.; Koski, K. J.; Deepak, F. L.; Ramasubramaniam, A.; Naveh, D. Optoelectronics of Atomic Metal-Semiconductor Interfaces in Tin-Intercalated MoS₂. *ACS Nano*, **2022**, *16*, 17080-17086.
- (36) Marseglia, E. A. Transition metal dichalcogenides and their intercalates. *Int. Rev. Phys. Chem.*, **1983**, *3*, 177-216.
- (37) Liu, X. C.; Zhao, S.; Sun, X.; Deng, L.; Zou, X.; Hu, Y.; Wang, Y. X.; Chu, C. W.; Li, J.; Wu, J.; Ke, F. S.; Ajayan, P. M. Spontaneous self-intercalation of copper atoms into transition metal dichalcogenides. *Sci. Adv.*, **2020**, *6*, aay4092.
- (38) Chrissafis, K.; Zamani, M.; Kambas, K.; Stoemenos, J.; Economou, N. A.; Samaras, I.; Julien, C. Structural Studies of MoS₂ Intercalated by Lithium. *Mat. Sci. Eng. B-Solid State Mater. Adv. Technol.*, **1989**, 3, 145-151.
- (39) Mulhern, P. J. Lithium Intercalation in Crystalline Li_xMoS₂. *Can. J. Phys.*, **1989**, *67*, 1049-1052.
- (40) Tsai, H. L.; Heising, J.; Schindler, J. L.; Kannewurf, C. R.; Kanatzidis, M. G. Exfoliated-restacked phase of WS₂. *Chem. Mater.*, **1997**, *9*, 879-882.
- (41) Petkov, V.; Billinge, S. J. L.; Larson, P.; Mahanti, S. D.; Vogt, T.; Rangan, K. K.; Kanatzidis, M. G. Structure of nanocrystalline materials using atomic pair distribution function analysis: Study of LiMoS₂. *Phys. Rev. B*, **2002**, 65, 092105.
- (42) Stern, C.; Twitto, A.; Snitkoff, R. Z.; Fleger, Y.; Saha, S.; Boddapati, L.; Jain, A.; Wang, M.; Koski, K. J.; Deepak, F. L.; Ramasubramaniam, A.; Naveh, D. Enhancing Light–Matter Interactions in MoS₂ by Copper Intercalation. *Adv. Mater.*, **2021**, 33, 2008779.
- (43) Chen, S.; Johnson, V. L.; Donadio, D.; Koski, K. J. Mn-intercalated MoSe₂ under pressure: Electronic structure and vibrational characterization of a dilute magnetic semiconductor. *J. Chem. Phys.*, **2020**, *153*, 124701.
- (44) Wang, M.; Al-Dhahir, I.; Appiah, J.; Koski, K. J. Deintercalation of Zero-Valent Metals from Two-Dimensional Layered Chalcogenides. *Chem. Mater.*, **2017**, 29, 1650-1655.
- (45) Divigalpitiya, W. M. R.; Frindt, R. F.; Morrison, S. R. Inclusion Systems of Organic-Molecules in Restacked Single-Layer Molybdenum-Disulfide. *Science*, **1989**, *246*, 369-371.
- (46) Tagaya, H.; Hashimoto, T.; Karasu, M.; Izumi, T.; Chiba, K. Inclusion of Substituted Ferrocenes and Aromatic-Compounds into MoS₂ Layers as New Intercalation Compounds. *Chem. Lett.*, **1991**, 2113-2116.
- (47) Golub, A. S.; Protzenko, G. A.; Yanovskaya, I. M.; Lependina, O. L.; Novikov, Y. N. New Intercalation Compounds of Molybdenum Disulfide with Transition Metals, $A_z(H_2O)_yMoS_2$ (A = Fe, Co, Ni, Y, La, Er, Th). *Mendeleev Commun.*, **1993**, 3, 199-200.
- (48) Kanatzidis, M. G.; Bissessur, R.; Degroot, D. C.; Schindler, J. L.; Kannewurf, C. R. New Intercalation Compounds of Conjugated Polymers Encapsulation of Polyaniline in MoS₂. *Chem. Mater.*, **1993**, *5*, 595-596.
- (49) Lemmon, J. P.; Lerner, M. M. Preparation and Characterization of Nanocomposites of Polyethers and Molybdenum-Disulfide. *Chem. Mater.*, **1994**, *6*, 207-210.
- (50) Bissessur, R.; Heising, J.; Hirpo, W.; Kanatzidis, M. Toward pillared layered metal sulfides. Intercalation of the chalcogenide clusters $Co_6Q_8(PR_3)_6$ (Q = S, Se, and Te and R = Alkyl) into MoS₂. Chem. Mater., **1996**, 8, 318-320.
- (51) Kosidowski, L.; Powell, A. V. Naphthalene intercalation into molybdenum disulfide. *Chem. Commun.*, **1998**, 2201-2202.

- (52) Dungey, K. E.; Curtis, M. D.; Penner-Hahn, J. E. Structural characterization and thermal stability of MoS₂ intercalation compounds. *Chem. Mater.*, **1998**, *10*, 2152-2161.
- (53) Saada, I.; Bissessur, R. Nanocomposite materials based on chitosan and molybdenum disulfide. *J. Mater. Sci.*, **2012**, *47*, 5861-5866.
- (54) Jeffery, A. A.; Nethravathi, C.; Rajamathi, M. Two-Dimensional Nanosheets and Layered Hybrids of MoS₂ and WS₂ through Exfoliation of Ammoniated MS₂ (M = Mo₂W). *J. Phys. Chem. C*, **2014**, *118*, 1386-1396.
- (55) Jeffery, A. A.; Nethravathi, C.; Rajamathi, M. Scalable large nanosheets of transition metal disulphides through exfoliation of amine intercalated MS₂ [M = Mo, W] in organic solvents. RSC Adv., **2015**, 5, 51176-51182.
- (56) Acerce, M.; Voiry, D.; Chhowalla, M. Metallic 1T phase MoS₂ nanosheets as supercapacitor electrode materials. *Nat. Nanotechnol.*, **2015**, *10*, 313-318.
- (57) Meza, E.; Diaz, R. E.; Li, C. W. Solution-Phase Activation and Functionalization of Colloidal WS₂ Nanosheets with Ni Single Atoms. ACS Nano, **2020**, 14, 2238-2247.
- (58) Hong, W.; Meza, E.; Li, C. W. Controlling the Co-S coordination environment in Co-doped WS₂ nanosheets for electrochemical oxygen reduction. *J. Mater. Chem. A*, **2021**, *9*, 19865-19873.
- (59) Kuo, D. Y.; Cossairt, B. M. Direct intercalation of MoS₂ and WS₂ thin films by vacuum filtration. *Mater. Horiz.*, **2022**, *9*, 360-367.
- (60) Kuo, D. Y.; Rice, P. S.; Raugei, S.; Cossairt, B. M. Charge Transfer in Metallocene Intercalated Transition Metal Dichalcogenides. *J. Phys. Chem. C*, **2022**, *126*, 13994-14002.
- (61) Zeng, Z.; Yin, Z.; Huang, X.; Li, H.; He, Q.; Lu, G.; Boey, F.; Zhang, H. Single-layer semiconducting nanosheets: High-yield preparation and device fabrication. *Angew. Chem. Int. Ed.*, **2011**, *50*, 11093-11097.
- (62) Enyashin, A. N.; Yadgarov, L.; Houben, L.; Popov, I.; Weidenbach, M.; Tenne, R.; Bar-Sadan, M.; Seifert, G. New Route for Stabilization of 1T-WS₂ and MoS₂ Phases. *J. Phys. Chem. C*, **2011**, *115*, 24586-24591.
- (63) Wypych, F.; Schollhorn, R. 1T-MoS₂, a New Metallic Modification of Molybdenum-Disulfide. *J Chem Soc Chem Comm*, **1992**, 1386-1388.
- (64) Han, A. L.; Zhou, X. F.; Wang, X. J.; Liu, S.; Xiong, Q. H.; Zhang, Q. H.; Gu, L.; Zhuang, Z. C.; Zhang, W. J.; Li, F. X.; Wang, D. S.; Li, L. J.; Li, Y. D. One-step synthesis of single-site vanadium substitution in 1T-WS₂ monolayers for enhanced hydrogen evolution catalysis. *Nat. Commun.*, **2021**, *12*, 709.
- (65) Sekine, T., Nakashizu, T., Toyoda, K., Uchinokura, K., Matsuura, E. Raman scaterring in layered compound 2H-WS₂. *Solid State Commun.*, **1980**, 35, 371-373.
- (66) Voiry, D.; Yamaguchi, H.; Li, J.; Silva, R.; Alves, D. C. B.; Fujita, T.; Chen, M.; Asefa, T.; Shenoy, V. B.; Eda, G.; Chhowalla, M. Enhanced catalytic activity in strained chemically exfoliated WS₂ nanosheets for hydrogen evolution. *Nat. Mater.*, **2013**, *12*, 850-855.
- (67) Liu, Q.; Li, X.; Xiao, Z.; Zhou, Y.; Chen, H.; Khalil, A.; Xiang, T.; Xu, J.; Chu, W.; Wu, X.; Yang, J.; Wang, C.; Xiong, Y.; Jin, C.; Ajayan, P. M.; Song, L. Stable Metallic 1T-WS₂ Nanoribbons Intercalated with Ammonia Ions: The Correlation between Structure and Electrical/Optical Properties. *Adv. Mater.*, **2015**, *27*, 4837-4844.
- (68) Qian, X., Liu, J., Li, J. Quantum spin Hall effect in two-dimensional transition metal dichalogenides. *Science*, **2014**, 346, 1344-1348.
- (69) Pierucci, D.; Zribi, J.; Livache, C.; Greboval, C.; Silly, M. G.; Chaste, J.; Patriarche, G.; Montarnal, D.; Lhuillier, E.; Ouerghi, A.; Mahler, B. Evidence for a narrow band gap phase in 1T 'WS2 nanosheet. *Appl. Phys. Lett.*, **2019**, *115*, 032102.
- (70) Mahler, B.; Hoepfner, V.; Liao, K.; Ozin, G. A. Colloidal synthesis of 1T-WS₂ and 2H-WS₂ nanosheets: Applications for photocatalytic hydrogen evolution. *J. Am. Chem. Soc.*, **2014**, *136*, 14121-14127.
- (71) Kopnov, F.; Feldman, Y.; Popovitz-Biro, R.; Vilan, A.; Cohen, H.; Zak, A.; Tenne, R. Intercalation of alkali metal in WS₂ nanoparticles, revisited. *Chem. Mater.*, **2008**, 20, 4099-4105.
- (72) Kumar, D.; Singh, B.; Kumar, P.; Balakrishnan, V.; Kumar, P. Thermal expansion coefficient and phonon dynamics in coexisting allotropes of monolayer WS₂ probed by Raman scattering. *J. Phys. Condens. Matter*, **2019**, 31, 505403.
- (73) Bae, S.; Matsumoto, K.; Raebiger, H.; Shudo, K.-i.; Kim, Y.-H.; Handegård, Ø. S.; Nagao, T.; Kitajima, M.; Sakai, Y.; Zhang, X.; Vajtai, R.; Ajayan, P.; Kono, J.; Takeda, J.; Katayama, I. K-point longitudinal acoustic

phonons are responsible for ultrafast intervalley scattering in monolayer MoSe₂. *Nat. Commun.*, **2022**, *13*, 4279.

- (74) Calandra, M. Chemically exfoliated single-layer MoS₂: Stability, lattice dynamics, and catalytic adsorption from first principles. *Phys. Rev. B*, **2013**, 88, 245428.
- (75) Ghosh, S.; Agarwal, H.; Galib, M.; Tran, B.; Balasubramanian, M.; Singh, N.; Fulton, J. L.; Govind, N. Near-Quantitative Predictions of the First-Shell Coordination Structure of Hydrated First-Row Transition Metal Ions Using K-Edge X-ray Absorption Near-Edge Spectroscopy. *J. Phys. Chem. Lett.*, **2022**, *13*, 6323-6330.
- (76) Levina, A.; McLeod, A. I.; Lay, P. A. Vanadium Speciation by XANES Spectroscopy: A Three-Dimensional Approach. *Chem-Eur. J.*, **2014**, *20*, 12056-12060.
- (77) Finger, L. W.; Hazen, R. M. Crystal-Structure and Isothermal Compression of Fe₂O₃,Cr₂O₃, and V₂O₃ to 50 Kbars. *J. Appl. Phys.*, **1980**, *51*, 5362-5367.
- (78) Kim, J. Y.; Choi, S. M.; Seo, W. S.; Cho, W. S. Thermal and Electronic Properties of Exfoliated Metal Chalcogenides. *Bull. Korean Chem. Soc.*, **2010**, *31*, 3225-3227.
- (79) Yao, J.; Koski, K. J.; Luo, W. D.; Cha, J. J.; Hu, L. B.; Kong, D. S.; Narasimhan, V. K.; Huo, K. F.; Cui, Y. Optical transmission enhancement

- through chemically tuned two-dimensional bismuth chalcogenide nanoplates. *Nat. Commun.*, **2014**, *5*, 5670.
- (80) Kelly, A. G.; Hallam, T.; Backes, C.; Harvey, A.; Esmaeily, A. S.; Godwin, I.; Coelho, J.; Nicolosi, V.; Lauth, J.; Kulkarni, A.; Kinge, S.; Siebbeles, L. D. A.; Duesberg, G. S.; Coleman, J. N. All-printed thin-film transistors from networks of liquid-exfoliated nanosheets. *Science*, **2017**, *356*, 69-73.
- (81) Nonnenmacher, M.; Oboyle, M. P.; Wickramasinghe, H. K. Kelvin Probe Force Microscopy. *Appl. Phys. Lett.*, **1991**, *58*, 2921-2923.
- (82) Melitz, W.; Shen, J.; Kummel, A. C.; Lee, S. Kelvin probe force microscopy and its application. *Surf. Sci. Rep.*, **2011**, *66*, 1-27.
- (83) Lee, N. J.; Yoo, J. W.; Choi, Y. J.; Kang, C. J.; Jeon, D. Y.; Kim, D. C.; Seo, S.; Chung, H. J. The interlayer screening effect of graphene sheets investigated by Kelvin probe force microscopy. *Appl. Phys. Lett.*, **2009**, *95*, 222107.
- (84) Filleter, T.; Emtsev, K. V.; Seyller, T.; Bennewitz, R. Local work function measurements of epitaxial graphene. *Appl. Phys. Lett.*, **2008**, 93, 133117.
- (85) Liu, Y.; Stradins, P.; Wei, S. H. Van der Waals metal-semiconductor junction: Weak Fermi level pinning enables effective tuning of Schottky barrier. *Sci. Adv.*, **2016**, *2*, 1600069.
- (86) Wang, X.; Dan, J.; Hu, Z.; Leong, J. F.; Zhang, Q.; Qin, Z.; Li, S.; Lu, J.; Pennycook, S. J.; Sun, W.; Sow, C. H. Defect Heterogeneity in Monolayer WS₂ Unveiled by Work Function Variance. *Chem. Mater.*, **2019**, *31*, 7970-7978.

Table of Contents artwork

